Phosphorus dual-site driven CoS$_2$@S, N co-doped porous carbon nanosheets for flexible quasi-solid-state supercapacitors

Shude Liu,[1] Daqiang Gao,[2] Junfu Li,[2] Kwan San Hui,[3] Ying Yin,*[1, 4] Kwun Nam Hui,*[5] and Seong Chan Jun*[1]

[1]School of Mechanical Engineering, Yonsei University, Seoul 120-749, South Korea.
[2]Key Laboratory for Magnetism and Magnetic Materials of MOE, Key Laboratory of Special Function Materials and Structure Design of MOE, Lanzhou University, Lanzhou, 730000, China.
[3]School of Mathematics, University of East Anglia, Norwich, NR4 7TJ, United Kingdom.
[4]Guangxi Key Laboratory of Information Materials, Guilin University of Electronic Technology, Guilin 541004, PR China.
[5]Institute of Applied Physics and Materials Engineering, University of Macau, Avenida da Universidade, Taipa, Macau, China.
*Corresponding author's E-mail: bizhui@umac.mo; yingguet@126.com; scj@yonsei.ac.kr

Abstract

Battery-type electrode materials typically suffer from intrinsically slow Faradaic reaction kinetics, which severely limits the energy and power density of supercapacitors. Herein, we develop a hybrid of P-doped CoS$_2$ (P-CoS$_2$) nanoparticles confined in a highly conductive P, S, N tri-doped carbon (P, S, N-C) porous nanosheets grown on carbon fiber through in situ thermal conversion of a metal–organic framework, followed by sulfurization and phosphorization. In this structural architecture, the heteroatom-enriched porous carbon nanosheets serve as a protective coating to inhibit the changes in the volume of the P-CoS$_2$ nanoparticles and offer

efficient pathways for rapid charge transfer. The nanosized P-CoS$_2$ substantially shortens the length of the electrolyte ion diffusion and shows enhanced covalency after the introduction of P atoms, resulting in decreased migration energy of electrons during the redox reaction. In particular, the P dopants exhibit improved electrical conductivity and reduced adsorption energy between OH$^-$ and the nuclear Co atoms in P-CoS$_2$, evidenced by density functional theory calculations. The designed P-CoS$_2$@P, S, N-C electrode possesses excellent rate capability and long-term cycling stability. Moreover, flexible solid-state asymmetric supercapacitor devices with P-CoS$_2$@P, S, N-C as the cathode and Co@P, N-C as the anode deliver a high energy density of 56.4 W h kg^{-1} at 725 W kg^{-1} and a capacitance retention of 94.1% over 5000 cycles at 20 A g^{-1}. The devices also exhibit uniform performance and outstanding bendability with slight capacitance decay under different bending conditions.

Introduction

High-efficiency energy storage systems have drawn considerable interest over the past decades because of the increasing demand for power supply in flexible and wearable electronics.[1] As an emerging candidate for electrochemical energy technologies, flexible supercapacitors have been extensively investigated due to their high power output, long cycle lifetime, and light weight.[2-4] However, the main bottleneck in using supercapacitors is the enhancement of their energy density to compete with rechargeable batteries without sacrificing the power density.[5] Transition metal sulfides

especially cobalt sulfides (e.g., CoS_2 and Co_9S_8), are attracting increasing attention as battery-like electrode materials for electrochemical energy storage owing to their higher electrochemical activity and redox reversibility compared with their corresponding transition metal oxides.[6-8] Nevertheless, the intrinsically slow ion diffusion and poor electronic conductivity of the battery-like materials restrict the electrode reaction kinetics, resulting in limited electrochemical properties.[9] To address these issues, scholars have adopted some feasible strategies, such as designing distinct structure architectures grown on conductive substrates, reducing the particle size, hybridizing with carbonaceous materials, and/or developing defect engineering.[10-12]

Metal-organic framework (MOF)-derived metal sulfide@carbon hybrids have gained great attention in electrochemical energy storage because they inherit the structural advantages of the precursors of the MOFs, such as well-defined porosity, ordered tunnels, and high specific surface area,[10, 13] and merge the features of high charge storage capability of metal sulfides and good rate performance of carbonaceous materials.[10, 14] Compared with conventional metal sulfide/surface-coated carbon planar hybrids, MOF-derived encapsulated hybrids with strong bridged bonds between the carbon matrix and active materials are more effective in maximizing the exposed active sites and improving cycling durability.[15] However, most MOF-derived hybrids are limited to agglomerated powders similar to those of their parent structures, leading to slow charge transfer kinetics and poor electrochemical stability.[16] An effective approach to resolve such drawbacks is the designing of MOFs grown on

highly conductive substrates,[17] especially with carbon fiber (CF) owing to its remarkable mechanical flexibility.[18] Importantly, constructing an integrated electrode configuration is conducive to increase the active surface area, boost electrical conductivity, and accelerate ion diffusion while avoiding the "dead volume" of the electrode materials from conducting additives or binders.[19]

Besides, anionic doping is regarded as another effective strategy to promote the reactive activity and improve the electrochemical performance of transition metal compounds because it can fundamentally regulate the electronic structure and alter the electron density.[20, 21] For example, pyrite-structured CoSP has recently been suggested as a hydrogen evolution electrocatalyst with improved catalytic activity and chemical stability due to partial substitution of S with P as a result of similar equilibrium volume of the cubic-phases of CoS_2 and CoP_2.[22] Similar study has shown that introducing P into O sites in Fe_2O_3 to strengthen the characteristic of predominant covalent bonds;[23] the process decreased the migration energy of the electrons, leading to the enhanced reactive reversibility and cycling stability for supercapacitor. Interestingly, several researches have also demonstrated that heteroatom doping and even multidoping (e.g., N, P, or S) engineering on carbonaceous materials can improve the specific capacitance by increasing the wettability, number of functional groups, and electronic structure of adjacent carbon atoms.[18, 24, 25] For instance, the incorporation of multi-heteroatom (N, O, and S) into the porous carbon efficiently promoted the electrochemical activity of carbon; a high

gravimetric capacitance of 306 F g^{-1} was achieved at a high current density of 1 A g^{-1} due to the enhanced electrical conductivity and polarizability along with the introduction of Faradaic reactions between the newly created functional groups and electrolyte ions.[26] Thus, a facile anionic regulation approach to enhance electrical properties and electrochemical reactivity of metal sulfide and carbon synthesized in MOF-derived hybrids is highly desirable but rarely reported.

Herein, we develop a facile strategy for in situ synthesis of P-doped CoS$_2$ nanoparticles encapsulated into P, S, and N tri-doped carbon matrix derived from Co-MOF nanosheets on the CF substrate. The integrated architecture with abundant mesopores and large open spaces provides abundant active sites and facilitates electron transfer, which is favorable for the reaction kinetics. The incorporation of P into CoS$_2$ also increases the degree of covalency, improves the electrical conductivity, and enhances the affinity between active sites and OH$^-$ in the electrolyte. As a result, P-CoS$_2$@P, S, N-C exhibits a large specific capacity of 689 C g^{-1} at 2 A g^{-1}, superior rate performance with 77.5% capacity retention at a high current density of 30 A g^{-1}, and long-term cyclability with 95.5% capacity retention after 5000 cycles. Furthermore, the flexible solid-state asymmetric supercapacitor (ASC) devices composed of P-CoS$_2$@P, S, N-C cathode and Co@P, N-C anode achieve an desirable energy density of 56.4 W h kg^{-1} at a power density of 725 W kg^{-1} and good cycling ability with only 5.9% capacitance loss after 5000 cycles at 20 A g^{-1}. After evaluation under different bending states, the ASC devices display excellent bendability with

essentially unchanged CV curves at 50 m V^{-1}. The voltage window and discharge time can be doubled upon coupling two ASC devices in series and parallel, respectively.

Results and discussion

The synthesis strategy for P-CoS$_2$@P, S, N-C porous nanosheets is schematically illustrated in Fig. 1. First, Co-MOF nanosheets were prepared using 2-methylimidazole (2-MeIm) and Co(NO$_3$)$_2$·6H$_2$O as reactants by a simple co-precipitation method at room temperature. Fig. S1a shows the X-ray diffraction (XRD) pattern of Co-MOF, which matches well with that of ZIF-67.[27] The morphology of Co-MOF was investigated using a scanning electron microscope (SEM). The Co-MOF nanosheets with uniform size distribution and smooth surface are aligned vertically and intercalated on the surface of the CF substrate (Fig. S2). The Co-MOF nanosheet precursor was pyrolyzed, in which organic ligands (MeIM) were transformed into carbon coordinated with N and the coordinated Co ions were in situ converted into metallic Co nanoparticles, forming a hybrid structure of Co@N-C. Co@N-C retains well the structural features of the Co-MOF precursor, except that the sheets show a rough surface (Fig. S3a and b). This finding is due to the formation of the porous structure during pyrolysis. The XRD pattern of Co@N-C (Fig. S1b) shows three main diffraction peaks that can be indexed to the face-centered cubic Co phase and other peaks that are ascribed to the characteristic graphitic peak of the carbon materials.[28] This result agrees with the energy-dispersive spectrometry (EDS) data

(Fig. S3c–h). On the one hand, phosphorization reaction was performed to convert the

Co@N-C into Co@P, N-C. On the other hand, a sulfurization reaction was conducted

on Co@N-C in the presence of sublimed sulfur to form the intact morphology of

CoS_2@S, N-C (Fig. S4a and b). The EDS elemental mapping of CoS_2@S, N-C (Fig.

S4c–h) verified the existence of Co, S, C, and N, and these elements are well

distributed in the carbon structure. Except for the broad peak at approximately 26.0°

corresponding to carbon, all other reflections of CoS_2@S, N-C (Fig. S5) can be

indexed to the CoS_2 pyrite phase (JCPDS: 41-1471).[29] A subsequent phosphorization

treatment was adopted to convert the CoS_2@S, N-C into P-CoS_2@P, S, N-C, as

evidenced by the XRD pattern (Fig. S5). Fig. 2a and b show that P-CoS_2@P, S, N-C

exhibits the hierarchical feature of the sheet units and possesses well-developed

macroporous structure. Compared with that of CoS_2@S, N-C, the nanosheet surface

of P-CoS_2@P, S, N-C becomes rough, which might be due to the anion exchange

from the nonequilibrium diffusion of different ion species during chemical

transformation.[27] The encapsulated hybrid with porous feature would provide rapid

electrolyte ion transport to the P-CoS_2 nanoparticles, while the carbon matrix mainly

stabilizes P-CoS_2 and improves the conductivity of the hybrid, leading to the high

utilization rate of P-CoS_2. The EDS results suggest the coexistence of Co, S, P, C, and

N (Fig. S6a–h). The transmission electron microscopy (TEM) images of P-CoS_2@P, S,

N-C shows that the P-CoS_2 nanoparticles are homogeneously embedded in the porous

graphene-like sheets (Fig. 2c). The nanoparticles were marked by green circles for

clear observation (Fig. 2d). The high resolution TEM (HRTEM) image of P-CoS_2@P,

S, N-C shows the lattice fringe spacings of 0.245 nm (Fig. 2e), which correspond to the interplanar distance of the (210) crystal plane of CoS_2. The occurrence of dim circles, rather than bright spots or circles, in the selected area electron diffraction (SAED) pattern (Fig. 2f) revealed the poor crystallinity of the hybrid structure,[30] consistent with the X-ray diffraction pattern in Fig. S5. The scanning TEM (STEM) image and corresponding mapping images from EDS indicate the homogeneous distribution of Co, N, S, C, and P in the whole nanosheet (Fig. 2g–m), with 2.88% P and 3.15% N. The measured Brunauer–Emmett–Teller (BET) specific surface area is 216.8 $m^2 g^{-1}$, and the total pore volume is 0.345 $cm^3 g^{-1}$ (Fig. S7). The isotherm of P-CoS_2@P, S, N-C displays a type-IV curve with an H1-type broad hysteresis loop, which implies the existence of mesoporous structures.[31] The high surface area and large pore volume facilitate the fast transport of the electrolyte ion for sufficient charge-transfer reaction, resulting in high electrochemical performance.

To analyze the surface chemistry and valence states of the as-synthesized samples, we conducted the X-ray photoelectron spectroscopy (XPS) analyses. The detected atomic ratio of C:N:S:Co in CoS_2@S, N-C is 75.05:3.91:14.21:6.83 using XPS measurement, and then the CoS_2 mass content of CoS_2@S, N-C is estimated to be about 47.3 wt%. For the Co2p spectra of CoS_2@S, N-C and P-CoS_2@P, S, N-C (Fig. 3a), the fitting peaks at 779.3 and 796.0 eV are assigned to Co^{3+}, while the other peaks at 781.6 and 779.7 eV are attributed to Co^{2+}.[32] Additional peaks at 778.0 and 792.9 eV were observed in the Co 2p spectrum of P-CoS_2@P, S, N-C and could be ascribed to the

presence of partially charged $Co^{\delta+}$ ($0<\delta<+2$) in the form of Co−P.[33] The Co 2p peak in

P-CoS$_2$@P, S, N-C shifts by approximately −0.4 eV compared with that of CoS$_2$@S,

N-C, indicating the reduced Co valance state caused by the newly formed Co-P after

the introduction of the P dopants. The S 2p spectra of CoS$_2$@S, N-C and P-CoS$_2$@P,

S, N-C (Fig. 3b) show that the two deconvoluted peaks at 162.7 and 163.8 eV are

indexed to the Co–S species,[34] while the peaks at 164.4 and 165.3 eV can be assigned

to S 2p$_{3/2}$ and S 2p$_{1/2}$ peaks from the –C–S–C– covalent bond, respectively.[35] S doping

is believed to increase the polarity of the carbon surface and reversible pseudosites

enhance the electrochemical property.[36] A peak at 169.0 eV corresponding to oxidized

S weakens after phosphorization, indicating that P doping can prevent the surface

oxidation of CoS$_2$. The finding is due to increased bond strength between Co and P/S

as a result of substitution of S by P in CoS$_2$, as revealed in recent literature.[22] The

asymmetric N 1s peaks (Fig. 3c) consist of four deconvoluted peaks at binding energy

levels of 398.5, 400.0, and 401.5 eV corresponding to pyridinic N, pyrrolic N, and

graphitic N, respectively.[33] These peaks illustrate the presence of N within the carbon

matrix. The pyridinic N with strong electron-accepting ability possesses an unshared

pair of electrons beside one electron donated to the conjugated π bond to facilitate the

introduction of electron donor properties to the materials.[37] The P 2p spectrum of

P-CoS$_2$@P, S, N-C consists of four peaks with binding energies at 129.3 (P 2P$_{3/2}$)

and 130.3 eV (P 2P$_{1/2}$) corresponding to the P–Co bonding ($P^{\delta-}$) as well as two other

peaks at 133.1 and 134.0 eV that are indexed to P−C and P–O, respectively.[33, 38] No

signal of P 2p was observed in CoS$_2$@S, N-C (Fig. 3d). This finding illustrates that

the P atoms have been successfully incorporated into CoS_2 and S, N-C after phosphorization to form $P-CoS_2@P$, S, N-C. The Raman spectra of $CoS_2@S$, N-C and $P-CoS_2@P$, S, N-C show two characteristic peaks at approximately 1347 cm^{-1} and 1585 cm^{-1} (Fig. S8), corresponding to the vibration modes of disordered graphite (D band) and E_{2g} of graphitized carbon (G band).[39] The I_D/I_G peak ratio of $P-CoS_2@P$, S, N (1.08) is larger than that of $CoS_2@S$, N-C (0.96), which indicates the presence of more disorders or defects within $P-CoS_2@P$, S, N-C.

Characterization and electrochemical properties of positive electrode materials

The electrochemical properties of the as-obtained electrodes were examined in a three-electrode configuration with a 2 M KOH aqueous electrolyte. Fig. 4a depicts the comparative cyclic voltammetry (CV) curves of $P-CoS_2@P$, S, N-C, and $CoS_2@S$, N-C at a scan rate of 100 mV s^{-1}. The $P-CoS_2@P$, S, N-C electrode exhibits a larger integral CV area than $CoS_2@S$, N-C, indicating the better electrochemical activities of $P-CoS_2@P$, S, N-C. The CF substrate negligibly contributes to the total stored charge of the $P-CoS_2@P$, S, N-C electrode (~1.94%) (Fig. S9). Two pairs of well-defined redox peaks can be observed in their CV curves, which could be assigned to the reversible Faradaic redox processes associated with the OH^- ions in the alkaline electrolyte as follows.[40]

$$CoS_2 + OH^- \leftrightarrow CoS_2OH + e^- \tag{1}$$

$$CoS_2OH + OH^- \leftrightarrow CoS_2O + H_2O + e^- \tag{2}$$
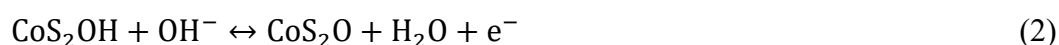
Electrochemical impedance spectroscopy (EIS) was performed (Fig. S10) to gain more insight into the enhanced electrochemical behavior of P-CoS$_2$@P, S, N-C. In the high-frequency region, the intercept at the x-axis in the EIS plots represents a combined resistance (R$_s$), including the intrinsic resistance of the electrode, ionic resistance of the electrolyte, and contact resistance between the active material and current collector.[41] The small depressed semicircle (R$_{ct}$) in the EIS plots can be ascribed to the charge transfer resistance at the electrolyte/electrode interface.[42] The R$_s$ and R$_{ct}$ of P-CoS$_2$@P, S, N-C are 0.28 and 0.29 Ω, respectively, which are lower than those of CoS$_2$@S, N-C (R$_s$=0.33 Ω and R$_{ct}$=0.59 Ω). This result suggests the superior electronic and ionic conductivity of P-CoS$_2$@P, S, N-C. Compared with that of CoS$_2$@S, N-C, the larger slope of the straight line in the EIS curve at the low-frequency region for P-CoS$_2$@P, S, N-C suggests improved capacitive behavior.[36]

The CV curves of CoS$_2$@S, N-C and P-CoS$_2$@P, S, N-C electrodes were recorded at different scan rates (Fig. 4b and S11). With increasing scan rate from 10 mV s^{-1} to 100 mV s^{-1}, the change of potential separation between the anodic and cathodic peaks of P-CoS$_2$@P, S, N-C (0.08 V from peak A to peak C; 0.16 V from peak B to peak D) is narrower than the corresponding value of CoS$_2$@S, N-C (0.09 V from peak A to peak C; 0.21 V from peak B to peak D). This characteristic implies the accelerated charge-transfer kinetics of P-CoS$_2$@P, S, N-C.[41] The relationship between the current response of the cathodic peak (I) and the scan rate (v) was explored by the power law of $I = a*v^b$ to elucidate the mechanism of charge storage of the as-synthesized

samples.[43, 44] The equation can be converted to $\log(I) = b\log(v) + \log(a)$. A b-value of 0.5 indicates complete diffusion-controlled reaction, while a b-value of 1 presents a surface capacitive-controlled process. The obtained b values for CoS_2@S, N-C (0.920 for peak C and 0.876 for peak D) and P-CoS_2@P, S, N-C (0.922 for peak C and 0.918 for peak D) electrodes are closer to 1 rather than 0.5, which indicates the typical surface-dominant capacitive process of the electrodes. Simon et al., Dunn et al., and Yuan et al. showed that most battery-type materials can potentially provide higher extrinsic pseudocapacitance and better pseudocapacitive behavior by increasing the electrochemical active sites, thereby reducing the particle size and/or the degree of crystallinity.[45-47] Furthermore, the b values corresponding to peaks C and D for P-CoS_2@P, S, N-C are larger than their counterparts for CoS_2@S, N-C, illustrating increased capacitive contribution ratio after the incorporation of P. The high surface capacitive contribution of P-CoS_2@P, S, N-C can be well correlated to its unique structural and compositional features (Fig. S13). (1) The 2D sheet-like morphology can not only offer sufficient electroactive surface sites for the redox reactions but also shorten the diffusion pathway of the electrolyte ion. (2) The void spaces between the vertically aligned nanosheets can be functionalized as electrolyte reservoirs for available electrolyte diffusion and effective mitigation of the change in volume upon cycling. (3) The active material integrated on the conductive substrate with chemical stable interface benefits from high electronic/ionic conductivities while efficiently avoiding the "dead mass" caused by multiple nonactive electrode additives (polymeric binder and carbon additive). (4) The synergetic function of the incorporated

heteroatoms on the electronic states of P-CoS$_2$ and P, S, N-C facilitates the electron transfer and promotes the reaction activity. (5) MOF-derived hybrids inherit the morphology of MOFs with high surface area, which facilitates the transport and diffusion of electrolyte ions, and the numerous voids between the P-CoS$_2$ nanoparticles and carbon matrix can help alleviate the volumetric expansion during the charge/discharge process; and (6) The incorporation of the P heteroatoms may lead to the reduced crystallinity due to the newly formed defects and disorder in P-CoS$_2$.

Fig. 4d shows the comparative galvanostatic charge-discharge (GCD) curves of CoS$_2$@S, N-C and P-CoS$_2$@P, S, N-C electrodes at a current density of 2 A g^{-1}. The discharge time of P-CoS$_2$@P, S, N-C is longer than that of CoS$_2$@S, N-C, consistent with the CV results. The GCD profiles of CoS$_2$@S, N-C and P-CoS$_2$@P, S, N-C electrodes at different current densities are shown in Fig. S12. The nonlinear GCD curves at different current densities illustrate the evident Faradaic behavior. The specific capacities of CoS$_2$@S, N-C and P-CoS$_2$@P, S, N-C electrodes are 435 C g^{-1} and 689 C g^{-1} at a current density of 2 A g^{-1}, respectively (Fig. 4e). With increasing current density up to 30 A g^{-1}, the P-CoS$_2$@P, S, N-C electrode still retains its initial capacity of 77.5%, which is superior to those of the CoS$_2$@S, N-C electrode (71.0%) and most of the recently reported Co-based electrodes for electrochemical supercapacitors.[48-50] The cycling performance of CoS$_2$@S, N-C and P-CoS$_2$@P, S, N-C electrodes is shown in Fig. 4f. After 5000 cycles at a current density of 30 A g^{-1},

the P-CoS$_2$@P, S, N-C exhibits a highly stable cycling ability with 95.5% retention of the initial capacity. The specific capacity of CoS$_2$@S, N-C drops rapidly, with the capacity retention of 86.3%. The long-term cycling stability of P-CoS$_2$@P, S, N-C is also superior to that of most of the reported Co-based nanostructures.[12, 50] The CoS$_2$@S, N-C and P-CoS$_2$@P, S, N-C electrodes deliver nearly 100% Coulombic efficiency after cycling (Fig. S14), which shows their high electrochemical reversibility.

To investigate the effect of P dopants on the electrochemical behavior of P-CoS$_2$, we studied the chemical bond characteristics that are associated with the electrode reaction kinetics.[51] The nature of the chemical bonds can be evaluated as follows: (%)=exp[−0.25(X_a−X_c)^2],[48, 51] where X_a and X_c are the electronegativity values of the anion and cation, respectively. Co has a Pauling electronegativity of 1.88, while that of S is 2.58 Pauling units and is higher than that of P (2.19). The covalent characteristics of Co-S and Co-P are determined to be 88.47% and 97.63%, respectively, revealing the enhanced degree of covalency by the substitution of S with P. As reported, the bond distance of Co–P (~2.26 Å) is longer than that of Co–S (~2.13 Å).[52, 53] The increased degree of covalency and bond distances of P-CoS$_2$ are favorable to improve the surface reactivity and electrode kinetics due to reduced energy required to extract electrons in the 3d orbitals of Co for the redox reactions.[54] In addition, heteroatom-doping into the carbon lattice can effectively boost the electrochemical behavior of carbonaceous materials due to the regulated electronic

properties and improved electrolyte wettability.[24, 26] The favorable complementarity of the tailored structural and electrical properties between P-CoS$_2$ and heteroatom-rich carbon leads to the high electrochemical performance.

To elucidate the underlying mechanism of P on the enhanced electrochemical performance of P-CoS$_2$, we performed density functional theory (DFT) calculations. Fig. S15a and b show the optimized ball-stick crystal models of CoS$_2$ and P-CoS$_2$ bulk. To investigate the effect of P dopants on the electron densities of the nearby atoms, the density of states and electronic band structures of CoS$_2$ and P-CoS$_2$ are displayed in Fig. 5a, b, S15c, and S15d. The P-CoS$_2$ exhibits obviously enhanced density of states at the conduction band edge compared with CoS$_2$. This change reveals that the incorporation of P atoms injects more electrons and improves the electrical conductivity of CoS$_2$. The calculated charge density distributions of CoS$_2$ and P-CoS$_2$ are shown in Fig. 5c and d. The distribution of the charge density around the P atom is more nonlocal after doping, which is conducive to the charge transfer with surrounding Co atoms, thereby accelerating the transfer rates of the surface charges for electrochemical reactions. Fig. 5e, f, and S16 show that the distance between the OH$^-$ and the nuclear Co atom site of the P-CoS$_2$ is approximately 1.82726 Å, which is shorter than that of CoS$_2$ (1.83256 Å), illustrating that the incorporation of P is conducive to the adsorbability of OH$^-$.[55] The inset in Fig. 1e and f depict that the calculated adsorption energy (E$_{ads}$) of OH$^-$ on P-CoS$_2$ is approximately −3.665 eV, which is lower than that on CoS$_2$ (detailed information is

shown in Table S1). This result further demonstrates the thermodynamically favorable adsorbability and stability of OH$^-$.[56] This finding is favorable to accelerate the redox reaction kinetics and enhance the electrochemical performance. The calculation results on the effect of P dopants are consistent with the experimental observations.

Characterization and electrochemical properties of negative electrode materials

The XRD pattern of Co@P, N-C shows that the two broad diffraction peaks at 25.5° and 43.5° are related to graphitic carbon, while the other peaks at 2θ=44.2°, 51.6°, and 76.0° are indexed to the cubic-phase metallic Co (Fig. S17).[25, 57] The embedded metallic nanoparticles can effectively increase the electrical conductivity of materials, leading to enhanced electrochemical activity.[58, 59] The low-magnification images in Fig. S18a and b show that vertically grown Co@P, N-C nanosheets are fully deposited on the surface of the CF substrate. The structural architecture of Co@P, N-C nanosheets is well preserved compared with that of Co@N-C, except that the surface becomes rough after phosphorization (Fig. 6a and b). The TEM images in Fig. 6c–e show that the metallic Co nanoparticles are embedded in the carbon nanosheets with abundant interconnected pores. The porous feature of Co@P, N-C was investigated by the N$_2$ adsorption–desorption isotherm and pore-size distribution results. Fig. S19a shows a typical type-IV isotherm with an obvious hysteresis loop, indicating a mesoporous structure of the carbon nanosheets.[38] The pore size distribution determined by the Barrett–Joyner–Halenda (BJH) method displays a peak centered at approximately 12 nm (Fig. S19b). The BET surface area and pore volume of Co@P,

N-C are $276.9 \ m^2 \ g^{-1}$ and $0.398 \ m^3 \ g^{-1}$, respectively. The structural characteristics would offer abundant active sites and favor the transmission and penetration of the electrolyte ions into the electrode. This process boosts the electrochemical reaction kinetics and contributes to the high capacitance. The HRTEM image of the Co@P, N-C shows the lattice fringes with d-spacing of 0.205 nm, corresponding to the (111) crystal plane of metallic Co (the inset in Fig. 5e). This result agrees with the XRD patterns. The EDS analysis of Co@P, N-C nanosheets confirms the presence of the N, P and Co elements in Co@P, N-C. The chemical states of the doped heteroatoms in the carbon matrix were further verified by XPS and Raman analyses (Fig. S20 and S21). The P, N co-doped carbon would be more efficient to regulate the surface properties and introduce more defects because of the synergistic effect of incorporating N and P.[38] This characteristic enhances the electrochemical reactivity.

Fig. S22 a and b show the typical CV curves of the Co@N-C and Co@P, N-C electrodes at different scan rates within the potential range from −1 V to −0.1 V (vs. SCE). The CV curves show quasi-rectangular shape and nearly symmetric current response on the voltage reversal, indicating their good capacitive behavior and desirable rate performance.[5] After phosphorization, the electrochemical reaction activity of Co@P, N-C is markedly improved, as shown by the enhanced CV area (Fig. 7a). The near triangular shape in the GCD curves of Co@N-C and Co@P, N-C electrodes illustrates their rapid I–V response.[5] As predicted, Co@P, N-C displays longer discharge time than Co@N-C (Fig. 7b). The specific capacitance as a function

of current density is shown in Fig. 7c. At a discharge current density of 1 A g^{-1}, the specific capacitance of Co@P, N-C is 283 F g^{-1}, which is superior to that of Co@N-C (161 F g^{-1}). Even with a 30-fold increase in the current density, the Co@P, N-C electrode still maintains 65.7% of its initial capacitance, which is higher than that of Co@N-C (58.1%). The cycling performance was evaluated at a current density of 1 A g^{-1} (Fig. 7d). The Co@P, N-C retains 270 F g^{-1} with only 6.4% deterioration of the initial specific capacitance after 5000 cycles. The specific capacitance of Co@N-C drops to 138 F g^{-1} despite its good cycling stability. The EIS measurements (Fig. S23) show that Co@P, N-C electrode possesses smaller R$_s$ (0.53 Ω) and R$_{ct}$ (0.31 Ω) than those of the Co@N-C electrode (R$_s$=0.72 Ω and R$_{ct}$=0.42 Ω). These results show the improved electrical conductivity and accelerated charge transfer. Such good electrochemical reactivity of Co@P, N-C could be attributed to heteroatom-induced electronic structure tuning, highly exposed active sites from well-defined porous structure, and fast electron transfer kinetics caused by the interaction between metallic Co nanoparticles and the carbon matrix.

Electrochemical properties and flexibility of asymmetric supercapacitors

To evaluate the potential of the as-constructed P-CoS$_2$@P, S, N-C//Co@P, N-C for real applications, flexible quasi-solid-state asymmetric supercapacitors (ASCs) were assembled by employing P-CoS$_2$@P, S, N-C as the cathode and Co@P, N-C as the anode using the poly (vinyl alcohol)/KOH (PVA/KOH) gel as the electrolyte, as schematically illustrated in Fig. 8a. The CV of the ASC device was performed at

different voltage windows at a scan rate of 50 mV s^{-1} (Fig. S24a). The operating

voltage window can be extended to 1.45 V, which is due to the full utilization of the

potential windows of the P-CoS$_2$@P, S, N-C and Co@P, N-C electrodes (Fig. S24b).

The CV curves of the ASC device at different scan rates from 10 mV s^{-1} to 100 mV

s^{-1} display obvious redox peaks (Fig. 8b), which are assigned to the occurrence of

Faradaic redox reactions. Moreover, no distinct shape distortion can be observed in

the CV curves at different scan rates. This phenomenon implies a fast rate

performance, which is attributed to the rapid ionic and electronic transport of

electrode materials.[60] Such nearly symmetric characteristics in the GCD curves

illustrate good electrochemical reversibility (Fig. 8c).[5]

To meet the specific energy and power demands, the device can be coupled in series

and parallel to increase the operating voltages and output currents with minimal

energy losses. When operating at a scan rate of 50 mV s^{-1}, two P-CoS$_2$@P, S,

N-C//Co@P, N-C ASCs connected in series deliver an output voltage twice that of a

single ASC, but the current response in the CV curve is nearly unchanged (Fig. 8d and

e). The enclosed CV curve is almost twice that of a single device when two ASCs are

integrated in parallel, while the operating voltage is unchanged. Furthermore, the

GCD curves of such two connected devices show that the output voltage for the

configuration combined in parallel and the discharging time for the configuration

combined in series are doubled relative to a single device at a current density of

$1 A g^{-1}$. These findings establish the high stability and programmability of the as-assembled integrated ASC devices.

Based on the total mass of active materials of the two electrodes, the specific capacitance of the P-CoS$_2$@P, S, N-C//Co@P, N-C ASC device are calculated to be $193 F g^{-1}$ at a current density of $1 A g^{-1}$ and retains $101 F g^{-1}$ at $20 A g^{-1}$ (Fig. S24c). Fig. 8f shows the Ragone plot relative to the energy and power densities of our fabricated ASCs compared with the recently reported ones. The ASC device stores the maximum energy density of $56.4 W h kg^{-1}$ at a power density of $725 W kg^{-1}$ and still maintains $29.5 W h kg^{-1}$ at a power density of $14,500 W kg^{-1}$ (equivalent to the discharge time of 7.4 s). The attained energy and power densities of the ASCs are superior to those of previously reported ASC devices, such as Co$_3$O$_4$@N-doped carbon//AC,[61] NiCoP/NiCo-OH//carbon,[62] NiO/Ni$_3$S$_2$//AC,[63] rGO/CoS$_2$/Ni$_3$S$_2$//rGO,[40] S-doped CoP//ZIF-8-derived carbon (ZIF-C)/rGO,[20] (Ni$_{0.1}$Co$_{0.9}$)$_9$Se$_8$//rGO,[64] and MnO$_2$@NiCo-LDH/CoS$_2$//AC.[65] The cycling performance of the ASC device was investigated at a high current density of $20 A g^{-1}$ over 5000 cycles (Fig. 8g). After the cycling test, the device retains approximately 94.1% of its initial capacitance while maintaining almost 97.0% Coulombic efficiency. Such high cycling stability of the assembled ASC device can be ascribed to the low charge transfer resistance and low ionic diffusion resistance, as verified by the EIS results (Fig. S24d and e). The image in Fig. 8h shows that two serially connected ASCs successfully drive a red light-emitting diode (LED, ~2V), indicating the good reproducibility of the connected

devices as power source. To verify the flexibility of the assembled quasi-solid-state ASC device, CV analyses under different flexed conditions were performed at a constant scan rate of 50 mV s^{-1} (the inset of Fig. 8i and S25). No noticeable change (within 4.5% fluctuation) can be detected in the CV curves (Fig. 8i), which indicates the outstanding mechanical flexibility of our devices. After the ASC has been flexed 500 times in the range of 0°−180°, the ASC still maintains 92.2% capacitance retention at a scan rate of 50 mV s^{-1} (Fig. S24f). The excellent flexibility might be ascribed to the robust deposition of the active material on the CF substrate that maintains the integrity of the electrode components.

Conclusions

In summary, we successfully designed and synthesized an encapsulated hybrid consisting of P-CoS$_2$ nanoparticles embedded into P, S, N-C nanosheets through pyrolysis, sulfurization, and phosphorization. The resultant hybrid structures with large surface area and high porosity provide many electrochemical active sites, short diffusion distance, and numerous channels for facile electrolyte ion access. Moreover, these devices possess integrated robust structure for a rapid electron transport. The incorporation of P increases the covalent character of CoS$_2$ that facilities the reduced energy required by electron migration during redox reactions. DFT calculations show that the introduced P dopants on P-CoS$_2$ can be used to tune the electronic structure and facilitate the adsorption of OH$^-$ to effectively enhance the redox reaction kinetics. The P-CoS$_2$@P, S, N-C hybrid enables a high specific capacity of 689 C g^{-1} at 2 A g^{-1},

excellent rate capability (77.5% retention at 30 A g^{-1}), and long-term cycling stability. Furthermore, flexible solid-state ASC devices based on P-CoS$_2$@P, S, N-C and Co@P, N-C exhibit a considerable energy density of 56.4 W h kg^{-1} at a power density of 725 W kg^{-1}, and an excellent stability with capacitance retention of 94.1% even after 5000 cycles at 20 A g^{-1}. The fabricated devices present an impressive flexibility, with no significant change in the specific capacitance under different bending conditions. The voltage window and discharge time are doubled for the two series- and parallel-connected ASC devices, respectively, which well agrees with the principal theorem of a capacitor in series and parallel combination. This anionic dual-site regulation strategy shows potential perspective to develop high-performance MOF-derived hybrids for future portable electronics devices.
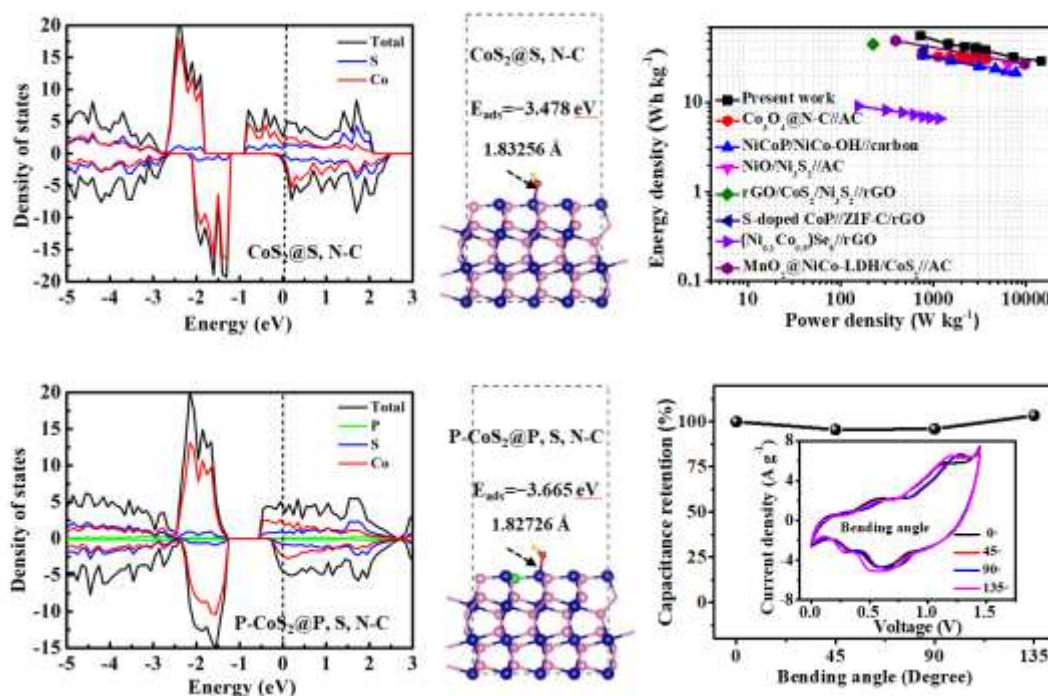
Conflict of interest

There are no conflicts to declare.

Acknowledgements

Graphical Abstract

An efficient P dual-site doping strategy is proposed to realize the synergistic regulation toward electrochemical active sites, electrical property, migration energy of electrons during the redox reaction, and adsorption energy between OH^- in the electrolyte and the active sites in P-CoS$_2$@P, S, N-C through a combined experimental and theoretical study. The P-CoS$_2$@P, S, N-C hybrid enables a high specific capacity of 689 C g^{-1} at 2 A g^{-1}, and excellent rate capability (77.5% retention at 30 A g^{-1}). Furthermore, the flexible solid-state ASC devices composed of P-CoS$_2$@P, S, N-C cathode and Co@P, N-C anode achieve an desirable energy density of 56.4 W h kg^{-1} at a power density of 725 W kg^{-1} and long-term cycling ability. Remarkably, the fabricated devices present an impressive flexibility, with no significant change in the specific capacitance under different bending conditions.
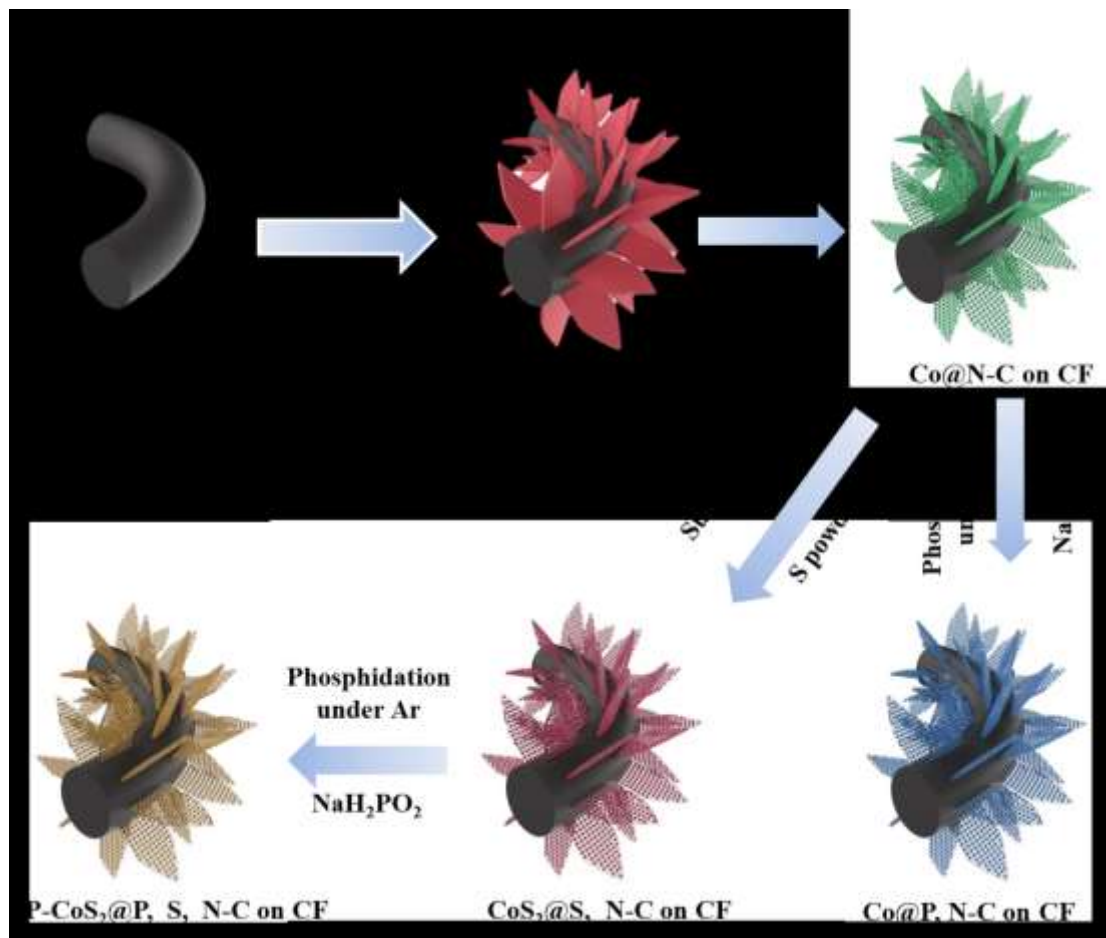
Figures

Fig. 1 Schematic illustration of fabrication for the P-CoS$_2$@P, S, N-C and Co@P, N-C nanosheets grown on the CF substrate.
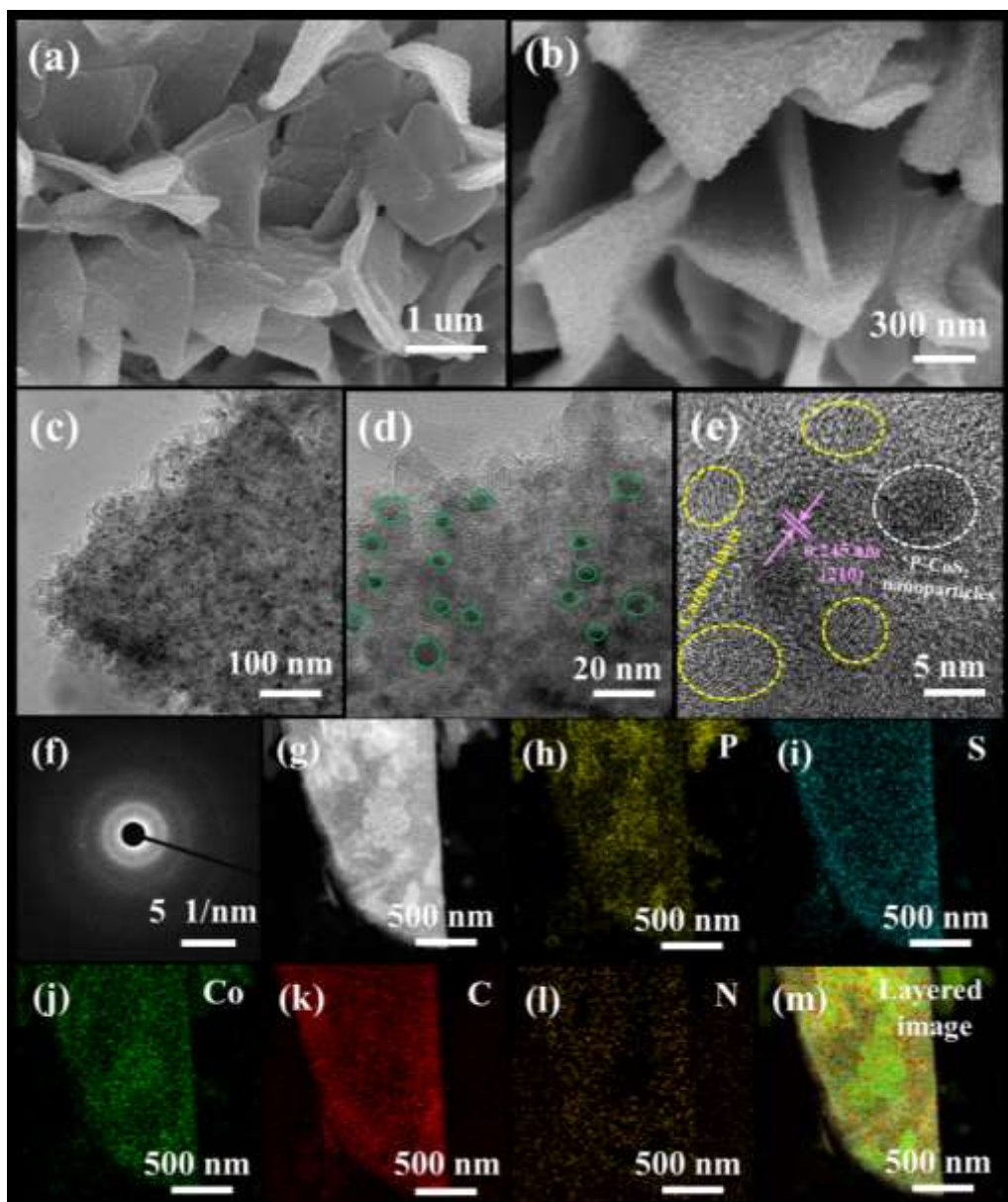
Fig. 2 Morphological characterization of the synthesized P-CoS$_2$@P, S, N-C nanosheets: (a, b) SEM images, (c, d) TEM images, (e) HRTEM image, (f) SAED pattern, and (g–m) STEM image and the corresponding EDS mappings of P, S, Co, C, and N.
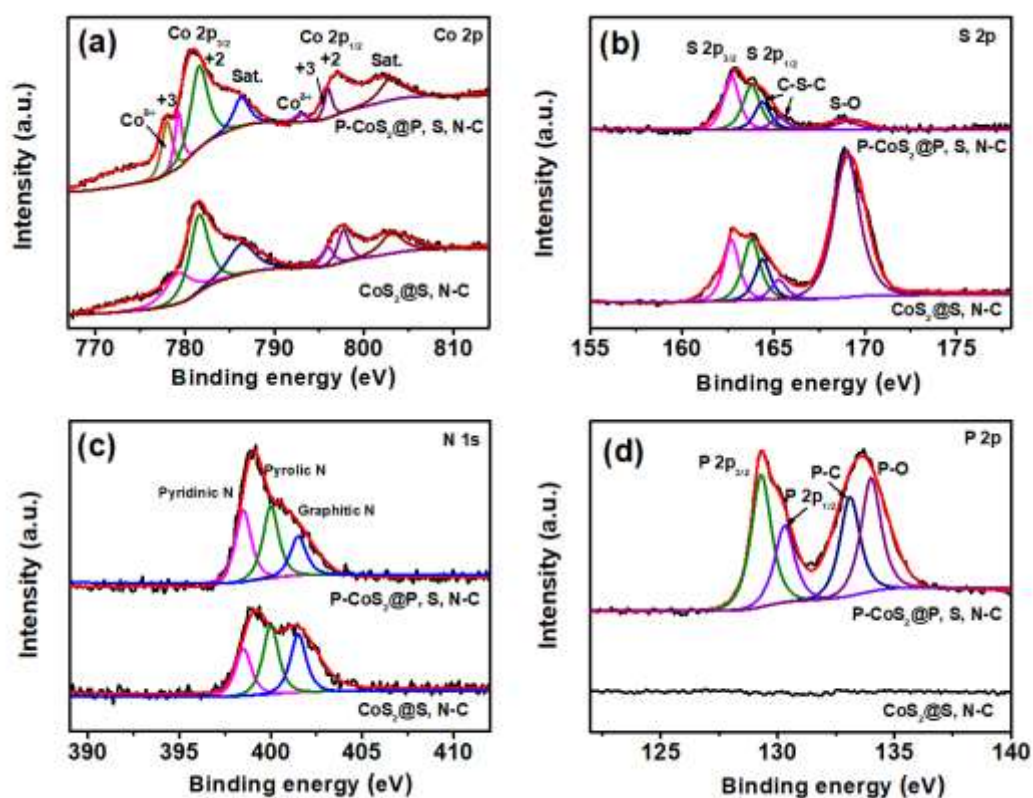
Fig. 3 High-resolution X-ray photoelectron spectra of (a) Co 2p, (b) S 2p, (c) N 1s, and (d) P 2p for the CoS_2@S, N-C and P-CoS_2@P, S, N-C nanosheets.
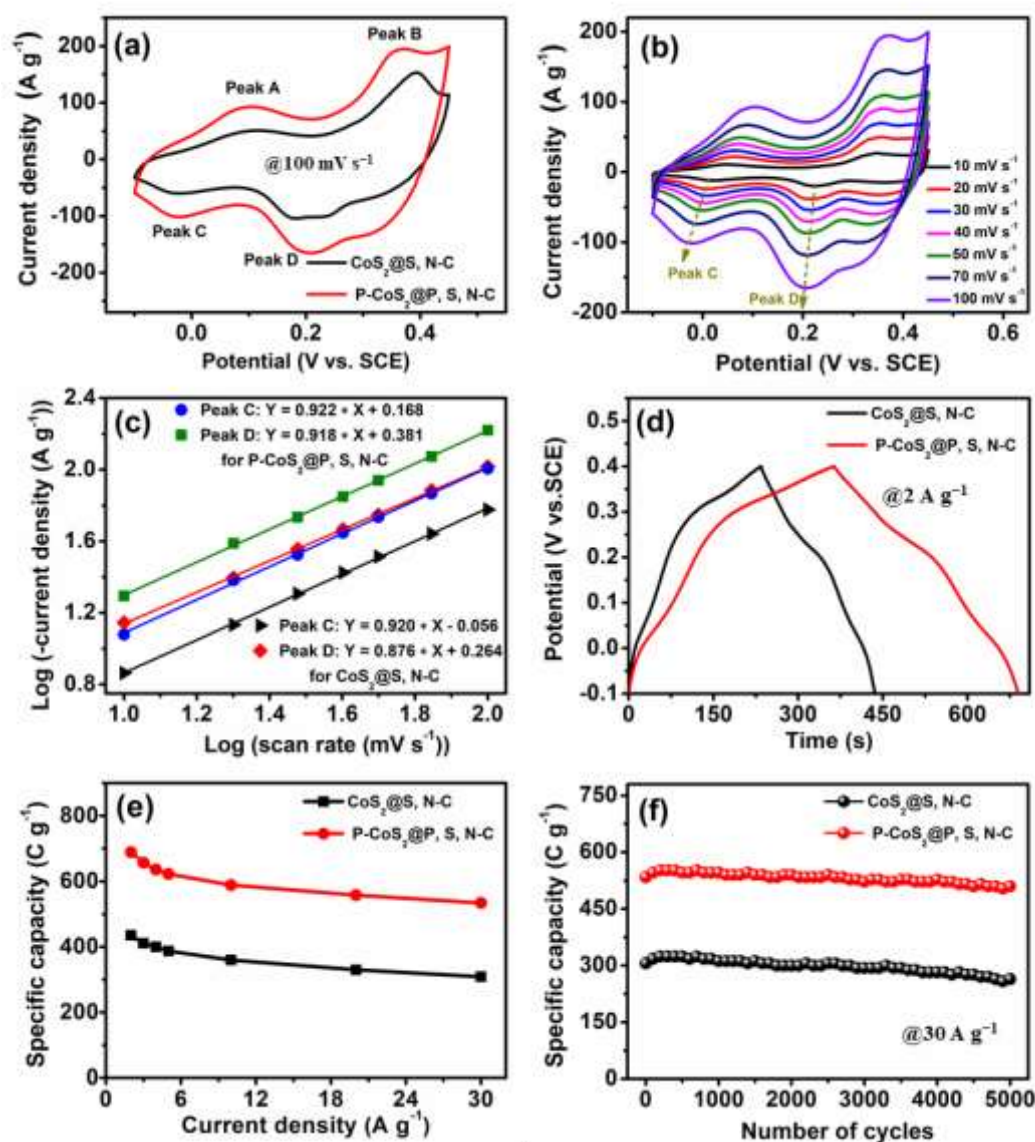
Fig. 4 (a) Comparative CV curves of CoS$_2$@S, N-C and P-CoS$_2$@P, S, N-C electrodes at a scan rate of 100 mV s^{-1}; (b) CV curves of P-CoS$_2$@P, S, N-C electrode at different scan rates; (c) Randles-Sevcik plots of CoS$_2$@S, N-C and P-CoS$_2$@P, S, N-C electrodes obtained from the CV curves; (d) comparative GCD profiles at the current density of 2 A g^{-1}; (e) specific capacities of CoS$_2$@S, N-C and P-CoS$_2$@P, S, N-C electrodes at various current densities; and (f) cycling performance of CoS$_2$@S, N-C and P-CoS$_2$@P, S, N-C electrodes at the current density of 30 A g^{-1}.
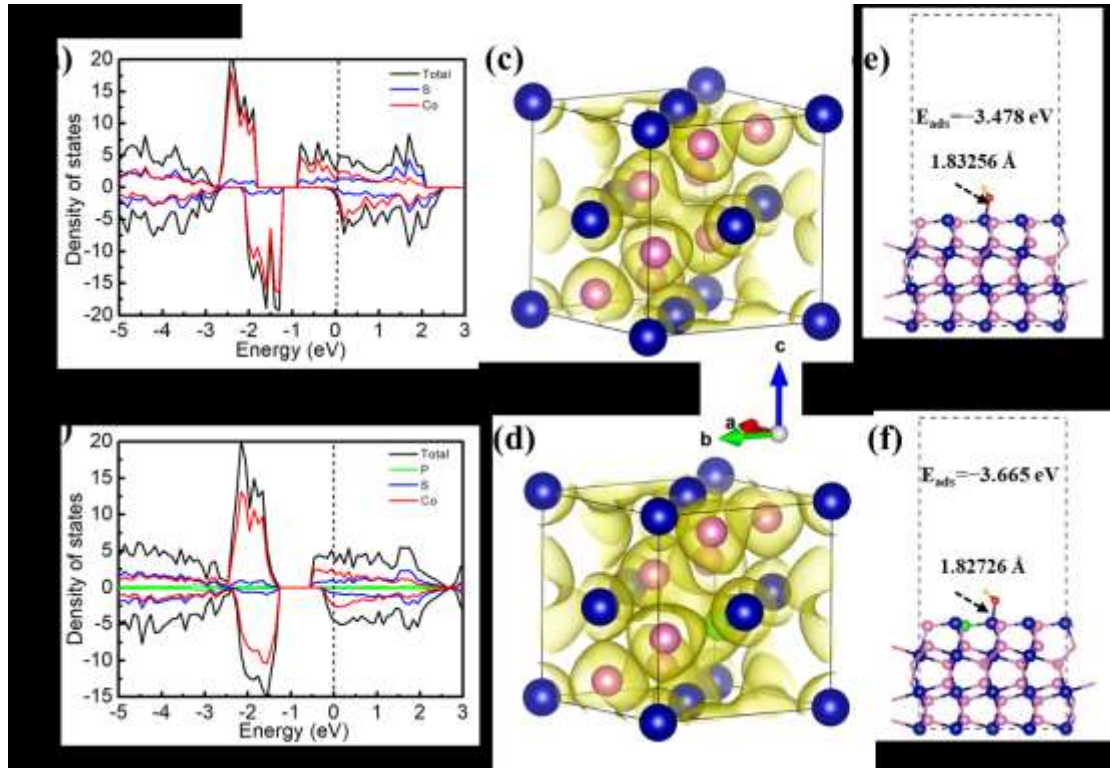
Fig. 5 Total and partial densities of states calculated for the (a) CoS_2 and (b) $P-CoS_2$ systems (the Fermi level is set to 0 eV); the local charge density distribution of the bulk (c) CoS_2 and (d) $P-CoS_2$; side view of the crystal structures [inset is $E_{ads}(OH^-)$ value] on the Co sites in the (100) slab of (e) CoS_2 and (f) $P-CoS_2$, where Co appears in blue, S in pink, P in green, O in red, and H in yellow.
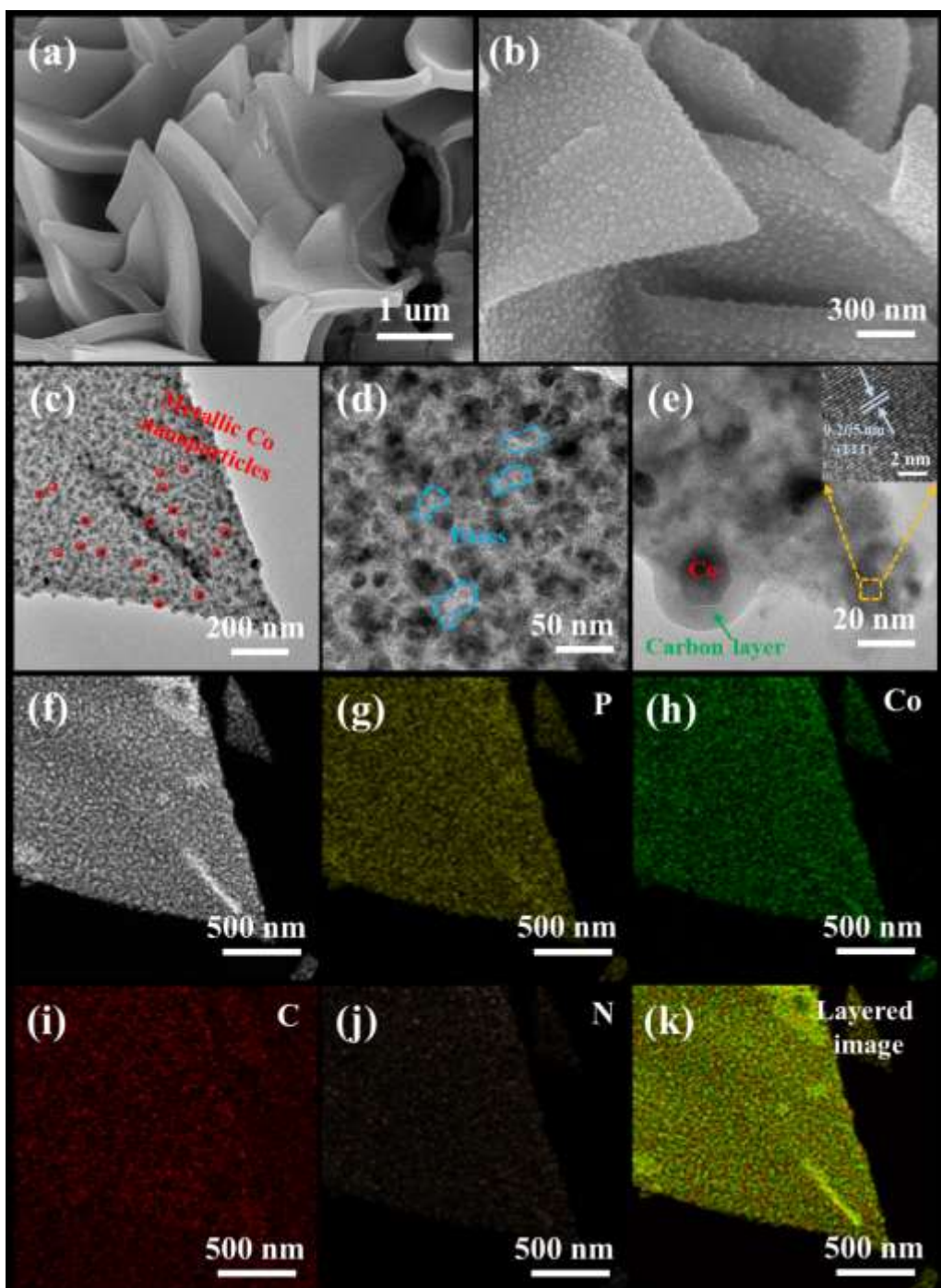
Fig. 6 Morphological characterization of the synthesized Co@P, N-C nanosheets: (a, b) SEM images, (c–e) TEM images and HRTEM image shown in the inset of the selected area in (e); (f–k) STEM image and the corresponding EDS mappings of P, Co, C and N.
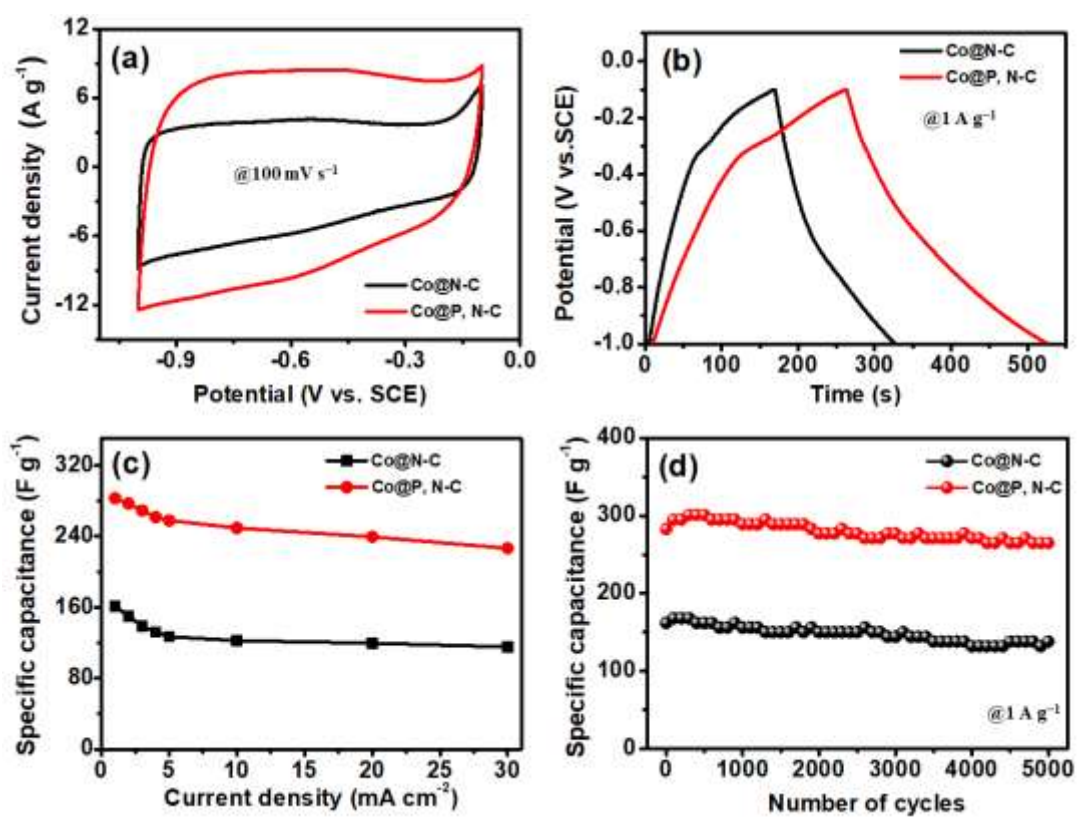
Fig. 7 (a) Comparison of the CV curves at a scan rate of 100 mV s^{-1}; (b) comparison of GCD curves at 1 A g^{-1}; (c) specific capacitance versus discharge current density; (d) cycling performance at a current density of 1 A g^{-1} for the Co@N-C and Co@P, N-C electrodes.
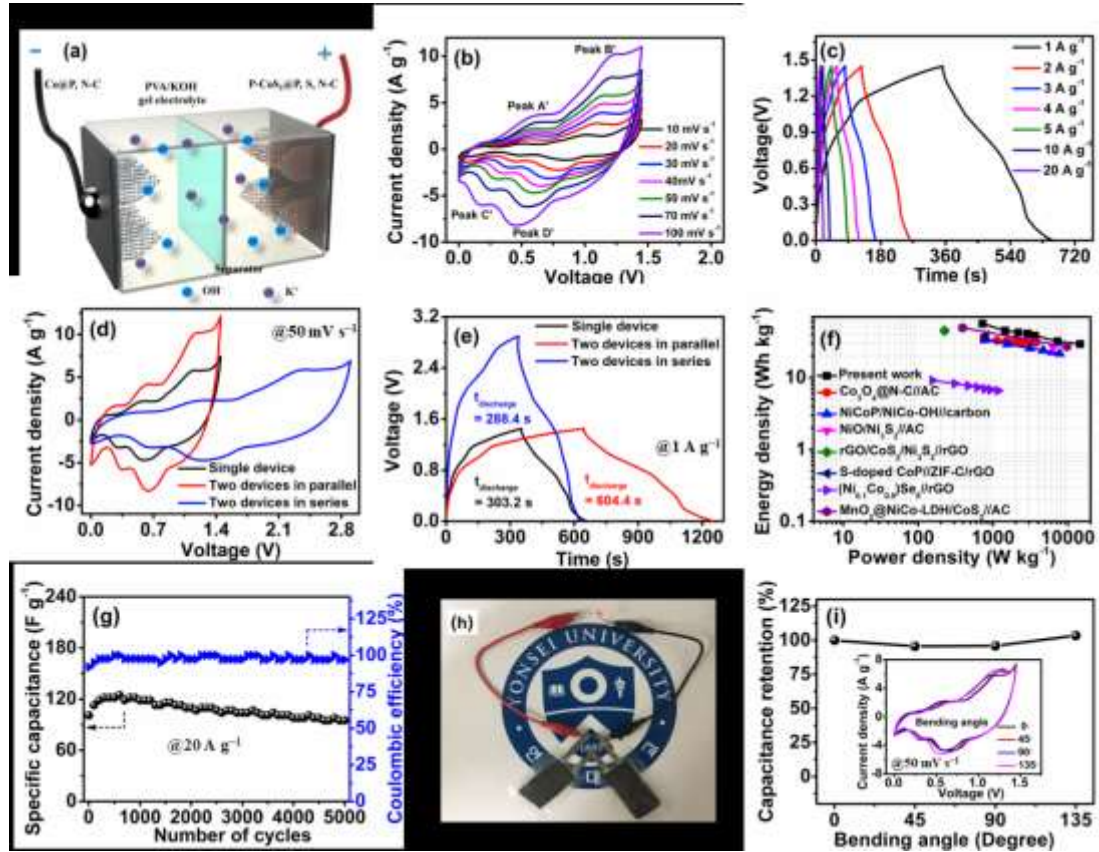
Fig. 8 (a) Schematic diagram of the as-fabricated P-CoS$_2$@P, S, N-C//Co@P, N-C ASC device; (b) CV profiles of the ASC device at different scan rates from 10 mV s^{-1} to 100 mV s^{-1}; (c) GCD curves of the ASC device at different current densities from 1 to 20 A g^{-1}; (d) CV curves of two as-assembled ASC devices in series or parallel connections at 50 mV s^{-1}; (e) GCD curves of two as-assembled ASC devices in series or parallel connections at 1 A g^{-1}; (f) Ragone plots of our fabricated ASC device compared with the reported ASC devices in the literature; (g) cycling stability and coulombic efficiency of the ASC device at a current density of 20 A g^{-1}; (h) photograph of an LED indicator powered by two P-CoS$_2$@P, S, N-C//Co@P, N-C ASC devices connected in series; and (i) capacitance retention of the ASC device at different bending angles (0°, 45°, 90°, and 135°). The inset is the comparative CV curves at 50 mV s^{-1} under different bending conditions.

Reference

1. L. Yao, Q. Wu, P. Zhang, J. Zhang, D. Wang, Y. Li, X. Ren, H. Mi, L. Deng and Z. Zheng, *Adv. Mater.*, 2018, **30**, 1706054.
2. X.-W. Lou, *Angew. Chem. Int. Ed.*, 2019, **10.1002/anie.201907516**.
3. L. Liu, Q. Dou, Y. Sun, Y. Lu, Q. Zhang, J. Meng, X. Zhang, S. Shi and X. Yan, *J. Mater. Chem. A*, 2019, **7**, 20398-20404.
4. X. Bu, L. Su, Q. Dou, S. Lei and X. Yan, *J. Mater. Chem. A*, 2019, **7**, 7541-7547.
5. Z. Pan, J. Yang, Q. Zhang, M. Liu, Y. Hu, Z. Kou, N. Liu, X. Yang, X. Ding and H. Chen, *Adv. Energy Mater.*, 2019, **9**, 1802753.
6. J. Yang, C. Yu, X. Fan, S. Liang, S. Li, H. Huang, Z. Ling, C. Hao and J. Qiu, *Energy Environ. Sci.*, 2016, **9**, 1299-1307.
7. J. Huang, J. Wei, Y. Xiao, Y. Xu, Y. Xiao, Y. Wang, L. Tan, K. Yuan and Y. Chen, *ACS Nano*, 2018, **12**, 3030-3041.
8. B. Y. Guan, L. Yu, X. Wang, S. Song and X. W. Lou, *Adv. Mater.*, 2017, **29**, 1605051.
9. Q. Dou, S. Lei, D.-W. Wang, Q. Zhang, D. Xiao, H. Guo, A. Wang, H. Yang, Y. Li and S. Shi, *Energy Environ. Sci.*, 2018, **11**, 3212-3219.
10. S. Sun, J. Luo, Y. Qian, Y. Jin, Y. Liu, Y. Qiu, X. Li, C. Fang, J. Han and Y. Huang, *Adv. Energy Mater.*, 2018, **8**, 1801080.
11. D. Su, S. Dou and G. Wang, *Adv. Energy Mater.*, 2015, **5**, 1401205.
12. S. Liu, Y. Yin, D. Ni, K. San Hui, K. N. Hui, S. Lee, C.-Y. Ouyang and S. C. Jun, *Energy Storage Mater.*, 2018, **19**, 186-196.
13. J. Zhao, H. Li, C. Li, Q. Zhang, J. Sun, X. Wang, J. Guo, L. Xie, J. Xie and B. He, *Nano Energy*, 2018, **45**, 420-431.
14. L. Shi, D. Li, P. Yao, J. Yu, C. Li, B. Yang, C. Zhu and J. Xu, *Small*, 2018, **14**, 1802716.
15. C. Yan, Y. Zhu, Z. Fang, C. Lv, X. Zhou, G. Chen and G. Yu, *Adv. Energy Mater.*, 2018, **8**, 1800762.
16. T. Rodenas, I. Luz, G. Prieto, B. Seoane, H. Miro, A. Corma, F. Kapteijn, F. X. L. i Xamena and J. Gascon, *Nat. Mater.*, 2015, **14**, 48.
17. M. Guo, J. Balamurugan, N. H. Kim and J. H. Lee, *Appl. Catal. B*, 2018, **239**, 290-299.
18. Y. Han, Y. Lu, S. Shen, Y. Zhong, S. Liu, X. Xia, Y. Tong and X. Lu, *Adv. Funct. Mater.*, 2018, **29**, 1806329.
19. C. Xia, Q. Jiang, C. Zhao, P. M. Beaujuge and H. N. Alshareef, *Nano Energy*, 2016, **24**, 78-86.
20. A. M. Elshahawy, C. Guan, X. Li, H. Zhang, Y. Hu, H. Wu, S. J. Pennycook and J. Wang, *Nano Energy*, 2017, **39**, 162-171.
21. S. Liu, Y. Yin, D. Ni, K. San Hui, M. Ma, S. Park, K. N. Hui, C.-Y. Ouyang and S. C. Jun, *Energy Storage Mater.*, 2019, **22**, 384-396.
22. W. Liu, E. Hu, H. Jiang, Y. Xiang, Z. Weng, M. Li, Q. Fan, X. Yu, E. I. Altman and H. Wang, *Nat. Commun.*, 2016, **7**, 1-9.

23. H. Liang, C. Xia, A.-H. Emwas, D. H. Anjum, X. Miao and H. N. Alshareef, *Nano Energy*, 2018, **49**, 155-162.

24. H. Hou, L. Shao, Y. Zhang, G. Zou, J. Chen and X. Ji, *Adv. Sci.*, 2017, **4**, 1600243.

25. Y. Gao, G. Hu, J. Zhong, Z. Shi, Y. Zhu, D. S. Su, J. Wang, X. Bao and D. Ma, *Angew. Chem. Int. Ed.*, 2013, **52**, 2109-2113.

26. M. Liu, J. Niu, Z. Zhang, M. Dou and F. Wang, *Nano Energy*, 2018, **51**, 366-372.

27. L. Yu, J. F. Yang and X. W. Lou, *Angew. Chem. Int. Ed.*, 2016, **55**, 13422-13426.

28. Y. Pan, K. Sun, S. Liu, X. Cao, K. Wu, W.-C. Cheong, Z. Chen, Y. Wang, Y. Li and Y. Liu, *J. Am. Chem. Soc.*, 2018, **140**, 2610-2618.

29. Y. Guo, L. Gan, C. Shang, E. Wang and J. Wang, *Adv. Funct. Mater.*, 2017, **27**, 1602699.

30. Y. Chen, Z. Li, Y. Zhu, D. Sun, X. Liu, L. Xu and Y. Tang, *Adv. Mater.*, 2019, **31**, 1806312.

31. K. Jayaramulu, J. Masa, O. Tomanec, D. Peeters, V. Ranc, A. Schneemann, R. Zboril, W. Schuhmann and R. A. Fischer, *Adv. Funct. Mater.*, 2017, **27**, 1700451.

32. L. Guo, J. Deng, G. Wang, Y. Hao, K. Bi, X. Wang and Y. Yang, *Adv. Funct. Mater.*, 2018, **28**, 1804540.

33. D. Das and K. K. Nanda, *Nano Energy*, 2016, **30**, 303-311.

34. N. Yao, P. Li, Z. Zhou, R. Meng, G. Cheng and W. Luo, *Small*, 2019, 1901993.

35. Y. Wang, Y. Zhang, J. Shi, A. Pan, F. Jiang, S. Liang and G. Cao, *J. Mater. Chem. A*, 2018, **6**, 18286-18292.

36. X. Dong, H. Jin, R. Wang, J. Zhang, X. Feng, C. Yan, S. Chen, S. Wang, J. Wang and J. Lu, *Adv. Energy Mater.*, 2018, **8**, 1702695.

37. P. Zhang, F. Sun, Z. Xiang, Z. Shen, J. Yun and D. Cao, *Energy Environ. Sci.*, 2014, **7**, 442-450.

38. S. Yang, L. Peng, P. Huang, X. Wang, Y. Sun, C. Cao and W. Song, *Angew. Chem. Int. Ed.*, 2016, **55**, 4016-4020.

39. X. Ren, Z. Ren, Q. Li, W. Wen, X. Li, Y. Chen, L. Xie, L. Zhang, D. Zhu and B. Gao, *Adv. Energy Mater.*, 2019, 1900091.

40. D. Jiang, H. Liang, W. Yang, Y. Liu, X. Cao, J. Zhang, C. Li, J. Liu and J. J. Gooding, *Carbon*, 2019, **146**, 557-567.

41. Q. Ke, C. Guan, X. Zhang, M. Zheng, Y. W. Zhang, Y. Cai, H. Zhang and J. Wang, *Adv. Mater.*, 2016, **29**, 1604164

42. Q. Zhang, Z. Liu, B. Zhao, Y. Cheng, L. Zhang, H.-H. Wu, M.-S. Wang, S. Dai, K. Zhang and D. Ding, *Energy Storage Mater.*, 2019, **16**, 632-645.

43. C. Zhao, C. Yu, M. Zhang, H. Huang, S. Li, X. Han, Z. Liu, J. Yang, W. Xiao and J. Liang, *Adv. Energy Mater.*, 2017, **7**, 1602880

44. L. Su, S. Lei, L. Liu, L. Liu, Y. Zhang, S. Shi and X. Yan, *J. Mater. Chem. A*, 2018, **6**, 9997-10007.

45. J. Sun, C. Wu, X. Sun, H. Hu, C. Zhi, L. Hou and C. Yuan, *J. Mater. Chem. A*, 2017, **5**, 9443-9464.

46. Y. Shao, M. F. El-Kady, J. Sun, Y. Li, Q. Zhang, M. Zhu, H. Wang, B. Dunn and R. B. Kaner, *Chem. Rev.*, 2018, **118**, 9233-9280.

47. X. Yu, S. Yun, J. S. Yeon, P. Bhattacharya, L. Wang, S. W. Lee, X. Hu and H. S. Park, *Adv. Energy Mater.*, 2018, **8**, 1702930.

48. S. Liu, Y. Yin, M. Wu, K. S. Hui, K. N. Hui, C. Y. Ouyang and S. C. Jun, *Small*, 2019, **15**, 1803984.

49. S. Liu, K. San Hui, K. N. Hui, H.-F. Li, K. W. Ng, J. Xu, Z. Tang and S. C. Jun, *J. Mater. Chem. A*, 2017, **5**, 19046-19053.

50. X. Wang, F. Huang, F. Rong, P. He, R. Que and S. P. Jiang, *J. Mater. Chem. A*, 2019, **7**, 12018-12028.

51. H. Liang, C. Xia, A.-H. Emwas, D. H. Anjum, X. Miao and H. N. Alshareef, *Nano Energy*, 2018, **49**, 155-162.

52. D.-H. Ha, L. M. Moreau, C. R. Bealing, H. Zhang, R. G. Hennig and R. D. Robinson, *J. Mater. Chem.*, 2011, **21**, 11498-11510.

53. Y. Shi, N. Zhang, Z. Gao, F. Kong and Q. Zhu, *J. Chem. Phys.*, 1994, **101**, 9528-9533.

54. T. Zhai, L. Wan, S. Sun, Q. Chen, J. Sun, Q. Xia and H. Xia, *Adv. Mater.*, 2017, **29**, 1604167.

55. S. Li, C. Yu, Y. Yang, X. Song, S. Chen, L. Song, B. Qiu, J. Yang, H. Huang and W. Guo, *Small*, 2018, **14**, 1803811.

56. J. Li, Z. Liu, Q. Zhang, Y. Cheng, B. Zhao, S. Dai, H.-H. Wu, K. Zhang, D. Ding and Y. Wu, *Nano Energy*, 2018, **57**, 22-33.

57. Q. Xiong, Y. Wang, P. F. Liu, L. R. Zheng, G. Wang, H. G. Yang, P. K. Wong, H. Zhang and H. Zhao, *Adv. Mater.*, 2018, **30**, 1801450.

58. Y. Zeng, Y. Meng, Z. Lai, X. Zhang, M. Yu, P. Fang, M. Wu, Y. Tong and X. Lu, *Adv. Mater.*, 2017, **29**, 1702698.

59. H. Lai, Q. Wu, J. Zhao, L. Shang, H. Li, R. Che, Z. Lyu, J. Xiong, L. Yang and X. Wang, *Energy Environ. Sci.*, 2016, **9**, 2053-2060.

60. J. Zhao, Z. Li, X. Yuan, Z. Yang, M. Zhang, A. Meng and Q. Li, *Adv. Energy Mater.*, 2018, **8**, 1702787.

61. T. Liu, L. Zhang, W. You and J. Yu, *Small*, 2018, **14**, 1702407.

62. X. Li, H. Wu, A. M. Elshahawy, L. Wang, S. J. Pennycook, C. Guan and J. Wang, *Adv. Funct. Mater.*, 2018, **28**, 1800036.

63. S. Liu, S. C. Lee, U. M. Patil, C. Ray, K. V. Sankar, K. Zhang, A. Kundu, J. H. Park and S. C. Jun, *J. Mater. Chem. A*, 2017, **5**, 4543-4549.

64. P. Yang, Z. Wu, Y. Jiang, Z. Pan, W. Tian, L. Jiang and L. Hu, *Adv. Energy Mater.*, 2018, **8**, 1801392.

65. X. Wang, F. Huang, F. Rong, P. He, R. Que and S. P. Jiang, *J. Mater. Chem. A*, 2019, **7**, 12018-12028.